Science & Technology Development Journal 2025, 28(3):3823-3832

Open Access Full Text Article

Research Article

Mechanistic insights into electrocatalytic carbon dioxide conversion to methane via carbon monoxide pathways on a PdCo catalyst

Huynh Tat Thanh[1,2,3], Viorel Chihaia[4], Do Ngoc Son[1,2,*]

ABSTRACT

The conversion of CO_2 into value-added products is of significant interest in mitigating greenhouse gas emissions and the global energy crisis. PdCo alloy is a promising catalyst for CO_2 conversion; however, no previous studies to date have focused on determining the reaction mechanisms and activity of the conversion of CO_2 to methane (CM conversion) on this alloy. To address this issue, in this study, we performed density functional theory calculations and thermodynamic analysis to explore CM conversion. Notably, CO poisoning is a key issue in transition metal catalysts; therefore, we focused on CM conversion via the CO formation pathway to establish whether the hydrogenation steps of CO succeed on the PdCo alloy. Our results revealed that hydrogenation processes are feasible with small thermodynamic barriers. Additionally, we gained physical insights into the interactions between the reaction intermediates and the PdCo catalyst.

Key words: Catalyst, Alloys, Computation, Modelling, Quantum Computing, CO poisoning.

[1]*Ho Chi Minh City University of Technology (HCMUT), 268 Ly Thuong Kiet Street, Dien Hong Ward, Ho Chi Minh City, Vietnam*

[2]*Vietnam National University Ho Chi Minh City, Linh Xuan Ward, Ho Chi Minh City, Vietnam*

[3]*An Giang University, VNU-HCM, 18 Ung Van Khiem street, Long Xuyen ward, An Giang Province, Vietnam*

[4]*Institute of Physical Chemistry "Ilie Murgulescu" of the Romanian Academy, Splaiul Independentei 202, Sector 6, 060021, Bucharest, Romania*

Correspondence

Do Ngoc Son, Ho Chi Minh City University of Technology (HCMUT), 268 Ly Thuong Kiet Street, Dien Hong Ward, Ho Chi Minh City, Vietnam

Vietnam National University Ho Chi Minh City, Linh Xuan Ward, Ho Chi Minh City, Vietnam

Email: dnson@hcmut.edu.vn

History

- Received: 28-03-2025
- Revised: 25-07-2025
- Accepted: 24-08-2025
- Published Online: 22-09-2025

DOI :

https://doi.org/10.32508/stdj.v28i3.4443

INTRODUCTION

The increasing CO_2 concentrations in the atmosphere due to fossil fuel usage have contributed significantly to global warming and anthropogenic climate change; therefore, CO_2 capture, conversion, and utilization processes are essential for addressing the problems posed by atmospheric CO_2 emissions. Among these processes, the conversion of CO_2 into fuels and fuel precursors (such as CO, CH_3OH, and CH_4) by using CO_2 as a carbon source represents a highly promising approach[1]. In terms of the valuable products obtained from CO_2 conversion, methane (CH_4) is particularly important due to its potential applications in power-to-gas technology and carbon capture and storage systems[1–4]. The conversion of CO_2 to CH_4 is based on thermochemical hydrogenation and the electrochemical reduction of CO_2; however, it is challenging to simultaneously achieve both high CO_2 conversion and high selectivity for a specific reaction product[1–4]. Furthermore, the operating conditions required for this conversion process are low temperature (around 300K) and relatively high pressure (about 30 bar)[1–4]. Another problem involved in the conversion process is catalyst stability, which is influenced by factors including catalyst degradation, poisoning, and precipitation[1–4]. Therefore, it is important to identify a catalyst with high stability that can be used to convert CO_2 to CH_4 under atmospheric conditions with high activity and selectivity[1].

Copper-based catalysts for CO_2 conversion, discovered 40 years ago by Hori et al.[5,6], continue to be intensively studied and improved using various approaches[7–9]. Obasanjo et al. created in situ activated Cu matrices to incorporate both dissolved CO_2 and CO_2 generated directly on the catalyst's surface from bicarbonate, which resulted in Faraday efficiencies above 70% and a CH_4 concentration of 23.5% in the product stream[10]. Other noble metals, such as Pt, have also been studied in a CO_2 conversion context; for example, Matsuda et al., using Pt-black in polymer membrane electrolysis without carbon support, produced CH_4 with a Faradaic yield of 23.2% at 0.18 V measured relative to a reversible hydrogen electrode (RHE) due to the high-density adsorbed CO and H[11]. Theoretical studies by Lu et al. showed that single-atom transition metal electrocatalysts anchored to antimonene monovacancies yield CH_4 as the main reaction product at a low overpotential of 0.5 V, with the interaction between the transition metal atom and the Sb monolayer via charge exchange shown to be the primary contributor to the increased catalytic activity of the CO_2 to CH_4 conversion (i.e., CM conversion)[12]. Organomolecular catalysts also have significant potential in CM conversion; for example, Xu et al. used a cluster membrane electrode based on 3,5-diamino-1,2,4-triazole to convert CO_2 to CH_4 with

Cite this article : Tat Thanh H, Chihaia V, Ngoc Son D. **Mechanistic insights into electrocatalytic carbon dioxide conversion to methane via carbon monoxide pathways on a PdCo catalyst**. *Sci. Tech. Dev. J.* 2025; 28(3):3823-3832.

VNUHCM PRESS

a Faradaic efficiency of 52±4% and a turnover frequency of 23,060 h^{-1} at 250 $mA.cm^{-2}$. Their results focused on the spatial distribution of catalytic sites and the formation of molecular orbitals with suitable energy levels for CM conversion [13].

Among the candidate CM conversion catalysts, Pd-alloy catalysts are considered particularly promising due to their excellent performance for both CO_2 hydrogenation and electrolysis to CH_4 [3]. Under ambient conditions, the main product for CO_2 hydrogenation catalyzed by monometallic Pd catalysts is CO, whereas alloy or intermetallic Pd catalysts have high selectivity for CH_3OH and CH_4. Iwasa et al. reported that monometallic Pd catalysts showed high CO formation only, whereas CO_2 hydrogenation via bimetallic Pd produced CH_3OH and CH_4 [14]. Jiang et al. showed that Pd nanoparticles embedded inside a UiO-66 support can catalyze CO_2 methanation with a CO_2 conversion of 56.0% and CH_4 selectivity of 97.3% [15]. In addition, Luo et al. found that intermetallic PdFe nanocrystals can achieve high CO_2 conversion, CH_4 selectivity, and catalytic stability, where the Fe surface promoted the direct dissociation of CO_2 to CO as an intermediate for CO_2 hydrogenation [16]. Pd-based catalysts can also be used for the electrochemical reduction of CO_2 to CH_4 in aqueous solution [3]. Zhu et al. reported that the reaction product of a pure Pd catalyst in aqueous solution is CO, an identical outcome to conventional CO_2 hydrogenation by Pd; however, the primary product of CO_2 electroreduction over $PdCu_3$ is CH_4, with a CH_4 current density seven times higher than that achieved using a state-of-the-art Cu catalyst [17]. Pd skin/PdCo alloys have also been identified as excellent catalysts for several reactions, including CO_2 conversion [14,18–22]. Based on experimental study, Snyder et al. suggested that PdCo alloy could be a promising catalyst for CO_2 conversion to formate via electroreduction with low overpotential and CO poisoning [23].

We recently explored CO_2-to-CH_3OH conversion on PdCo alloy with subsurface Co layers [22]. Our findings revealed that PdCo alloy represents a good catalyst for this conversion process; however, there are several possible by-products, including HCOOH and CO. Given that CO may cause catalyst poisoning in CO_2 conversion, it is essential to further explore CO_2 conversion via CO intermediates to weakly adsorbed products such as CH_4. Furthermore, the formation of the CO intermediate in the CO_2 conversion process is the rate-limiting step in the formation of other organic products [24–27], which thus inspired us to explore CO_2-to-CH_4 conversion via the CO pathway. In this study, we employed density functional theory (DFT) and a thermodynamics model to investigate the catalytic activity of PdCo alloy in the conversion of CO_2 to CH_4 via a CO intermediate.

METHODS

Our DFT calculations were performed using the Vienna ab initio simulation package (VASP) via the projector-augmented wave method with a cut-off energy of 400 eV [28–30]. The GGA PBE functional was employed to calculate the exchange-correlation energy [31]. The Methfessel–Paxton smearing method [32] with an energy width of 0.20 eV was used for structural optimization and vibrational analysis, while the tetrahedron method with Blöchl corrections [33] was used for total energy and electronic structure calculations. We sampled the Brillouin zone using a 5×5×1 Monkhorst–Pack mesh [34], which we tested for convergence with respect to structural optimization and total energy calculations.

We modeled the PdCo catalyst using a five-layer $p(4\times4)$ Pd(111) surface with a subsurface Co layer, referred to as the Pd-skin layer/PdCo alloy model (Figure 1). A detailed description of the slab model is provided in our previous study [22]. For further details of the optimization process and the characteristics of this PdCo alloy model, the reader is referred to the following studies [19,35,36].

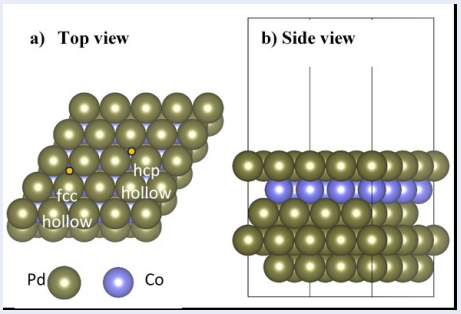

Figure 1: Illustration of a supercell of the PdCo alloy in the slab model; here, the fcc and hcp hollow sites are those with and without a Co atom underneath, respectively.

The CM conversion process via electro-catalysis was investigated in this study by constructing a Gibbs free energy diagram within the computational hydrogen electrode model [37]. The effect of proton-coupled electron transfer was determined via the reversible hydrogen electrode, resulting in $\frac{1}{2}H_2 \leftrightharpoons H^+ + e^-$. Overall, the Gibbs free energy change ($\triangle G$) of each elementary reaction step was calculated by

$$\triangle G = \triangle E - \triangle E_{ZPE} - T\triangle S + \triangle G_{pH} + \triangle G_U \quad (1)$$

where $\triangle E$, $\triangle E_{ZPE}$ and $\triangle S$ represent the total DFT reaction energy change, zero-point energy change, and the entropy change between products and reactants, respectively. Normal mode analysis was performed to determine the vibrational properties of the adsorbates and confirm their locally stable states. $\triangle G_{pH}$ is the contribution of the H^+ concentration, which is 0 at pH = 0. The contribution of the electrode potential, ΔG_U, is defined as

$$\triangle G_U = meU \quad (2)$$

where U is the applied electrode potential and m is the number of electrons exchanged during the reaction. The surface charge component can be included using various approaches, such as via direct DFT calculations or as $\triangle G_U$, as in equations (1) and (2). In this study, we chose the latter approach because it is easy to implement and has been previously verified.

The adsorption strength of the intermediates on the catalyst surface was evaluated based on the adsorption energy (E_a) as

$$E_a = E_{ads/S} - E_S - E_{ads} \quad (3)$$

Here $E_{ads/S}$, E_S, E_{ads} are the total energies of (i) the intermediate + PdCo system, (ii) the clean substrate, and (iii) the isolated adsorbate, respectively.

To determine the adsorbate–surface interactions, we calculated the charge density difference, which is defined as:

$$\triangle\rho = \rho_{ads/S} - \rho_{ads} - \rho_S \quad (4)$$

where $\rho_{ads/S}$, ρ_S *and* ρ_{ads} are the charge densities of (i) the intermediate + PdCo system, (ii) the clean substrate in the adsorbed state, and (iii) the isolated intermediate in the adsorbed state, respectively. We also performed Bader charge analysis to quantify the charge transfer interaction.

RESULTS AND DISCUSSION

Reaction pathway and intermediate stability

The overall equation of the CM conversion process is as follows:

$$CO_2 + 4H_2 \rightarrow CH_4 + 2H_2O \quad (R1)$$

The proposed reaction intermediates and reaction pathways on the surface of the PdCo catalyst are shown in Figure 2. Asterisks indicate intermediates that are in an adsorption state. The CM conversion proceeds via eight hydrogenation processes. Here, we modeled the hydrogenation process by adding an H atom to the adsorbed intermediate and then performed structural optimization using the DFT method to obtain a locally stable product state (Section 2). Vibrational analysis was then performed to validate the product's adsorption configuration, which must have no imaginary frequencies.

In Figure 2, CO_2 in the gaseous phase can adsorb on the PdCo substrate surface to generate CO_2*, which can either dissociate into CO*+O* or hydrogenate to form adsorbed carboxyl (COOH*). Hydrogenation of the O* atom of CO*+O* and the dissociation of COOH* will lead to the formation of CO*+OH*. In addition, hydrogenation of OH* in COOH* and CO*+OH* will convert these intermediates into CO*+H_2O*. Note that the water molecule was omitted in Figure 2 for simplicity. The other intermediates of the CM conversion are formed in subsequent hydrogenation steps, with CH_4 as the final product of the whole process. The 25 intermediate reaction steps are presented in full in , where the detailed components for the intermediates are accompanied by an asterisk on the right side of each intermediate step. Some of the intermediates related to the CM conversion process, including CO_2*, COOH*, CO*+H_2O*, COH*+H_2O*, HCO*+H_2O*, HCOH*+H_2O*, H_2CO*+H_2O*, CH_2OH*+H_2O*, and CH_3O*+H_2O*, were also identified for the CO_2-to-CH_3OH conversion, as reported in our previous study[22]. The newly found intermediates for the CM conversion process are CO*+O*, CO*+OH*, C*+2H_2O*, CH*+2H_2O*, CH_2*+2H_2O*, CH_4*+O*+H_2O*, CH_3*+2H_2O*, CH_4*+OH*+H_2O*, and CH_4*+2H_2O*, which are investigated in detail below. After using DFT calculations to optimize the geometric structure at different locations on the PdCo substrate surface, we obtained the most favorable configuration and determined the most stable adsorption site for the newly found intermediates of the CM conversion, as shown in Figure 3 and Figure 4, with further information about the studied intermediates also presented in Table 2. Figure 2 is generally applicable to any catalytic surface, including Pd skin/PdCo alloy catalysts; however, for each catalytic surface, DFT optimization must be performed for the geometric structure of the possible intermediates on the surface. If the intermediates can be stably adsorbed on the surface, they can then be included in the final scheme; otherwise, they should be excluded. The mechanisms proposed here have also been validated experimentally in other works[38,39].

Based on equation (3), Table 2 shows that the adsorption energy of all the newly found intermediates is negative, thus implying that these intermediates favorably adsorb on the PdCo surface. Most of the

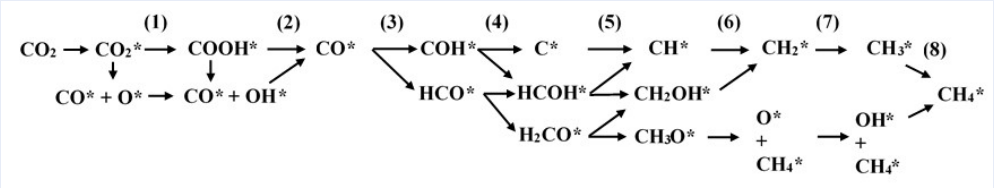

Figure 2: The proposed reaction pathways and intermediates for the CO_2-to-CH_4 conversion via CO formation

Table 1: Reaction equations for all intermediate steps of the CO_2 methanation process

Intermediate reaction steps	No.	Intermediate reaction steps	No
$CO_2 + 4H_2 + * \rightarrow CO_2^* + 4H_2$	(R2)	$C^* + 2H_2O^* + 2H_2 \rightarrow CH^* + 2H_2O^* + 3/2H_2$	(R15)
$CO_2^* + 4H_2 \rightarrow CO^* + O^* + 4H_2$	(R3)	$HCOH^* + H_2O^* + 2H_2 \rightarrow CH^* + 2H_2O^* + 3/2H_2$	(R16)
$CO_2^* + 4H_2 \rightarrow COOH^* + 7/2H_2$	(R4)	$HCOH^* + H_2O + 2H_2 \rightarrow CH_2OH^* + H_2O^* + 3/2H_2$	(R17)
$CO^* + O^* + 4H_2 \rightarrow CO^* + OH^* + 7/2H_2$	(R5)	$H_2CO^* + H_2O^* + 2H_2 \rightarrow CH_2OH^* + H_2O^* + 3/2H_2$	(R18)
$COOH^* + 7/2H_2 \rightarrow CO^* + OH^* + 7/2H_2$	(R6)	$H_2CO^* + H_2O^* + 2H_2 \rightarrow CH_3O^* + H_2O^* + 3/2H_2$	(R19)
$COOH^* + 7/2H_2 \rightarrow CO^* + H_2O^* + 3H_2$	(R7)	$CH^* + 2H_2O^* + 3/2H_2 \rightarrow CH_2^* + 2H_2O^* + H_2$	(R20)
$CO^* + OH^* + 7/2H_2 \rightarrow CO^* + H_2O^* + 3H_2$	(R8)	$CH_2OH^* + H_2O^* + 3/2H_2 \rightarrow CH_2^* + 2H_2O^* + H_2$	(R21)
$CO^* + H_2O^* + 3H_2 \rightarrow COH^* + H_2O^* + 5/2H_2$	(R9)	$CH_3O^* + H_2O^* + 3/2H_2 \rightarrow CH_4^* + O^* + H_2O^* + H_2$	(R22)
$CO^* + H_2O^* + 3H_2 \rightarrow HCO^* + H_2O^* + 5/2H_2$	(R10)	$CH_2^* + 2H_2O^* + H_2 \rightarrow CH_3^* + 2H_2O^* + 1/2H_2$	(R23)
$COH^* + H_2O^* + 5/2H_2 \rightarrow C^* + 2H_2O^* + 2H_2$	(R11)	$CH_4^* + O^* + H_2O^* + H_2 \rightarrow CH_4^* + OH^* + H_2O^* + 1/2H_2$	(R24)
$COH^* + H_2O^* + 5/2H_2 \rightarrow HCOH^* + H_2O^* + 2H_2$	(R12)	$CH_3^* + 2H_2O^* + 1/2H_2 \rightarrow CH_4^* + 2H_2O^*$	(R25)
$HCO^* + H_2O^* + 5/2H_2 \rightarrow HCOH^* + H_2O^* + 2H_2$	(R13)	$CH_4^* + OH^* + H_2O^* + 1/2H_2 \rightarrow CH_4^* + 2H_2O^*$	(R26)
$HCO^* + H_2O^* + 5/2H_2 \rightarrow H_2CO^* + H_2O^* + 2H_2$	(R14)		

newly identified intermediates in the CM conversion strongly bind to the PdCo surface due to the very large magnitudes of their adsorption energies, except for CH_4^*+$2H_2O^*$. In particular, the CO*+O* intermediate has an adsorption energy of -4.52 eV, the most negative adsorption energy among all intermediates, where CO* and O* are located at two different hcp hollow sites (top and side views in Figure 3a). The CO*+OH* intermediate has a similar adsorption site to that of CO*+O* (top and side views in Figure 3b), albeit with a smaller adsorption energy magnitude (Table 2). The C*+$2H_2O^*$ intermediate is strongly adsorbed on PdCo with a binding strength of -4.09 eV, where C^* is located at the fcc hollow site and the H_2O^* molecules are positioned around it (top and side views in Figure 4a). Further hydrogenation of C^* to form CH^* leads to a slightly more stable adsorption state of CH*+$2H_2O^*$ with an E_a of -4.36 eV compared to the -4.09 eV of C*+$2H_2O^*$. The fcc hollow is the stable adsorption site for CH* (top and side views in

Figure 4). In contrast, the next two hydrogenation steps, which Torm CH_2*+2H_2O* and CH_3*+2H_2O*, result in reduced binding strengths of 3.10 and 1.42 eV, respectively. The CH_2* and CH_3* intermediates are stably adsorbed at the bridge and top sites, respectively (top and side views in Figure 4c and Figure 4d). Furthermore, CM conversion via the CH_3O^* intermediate requires the formation of CH_4* +O*+H_2O* and CH_4*+OH*+H_2O*. We found that the O^* and OH^* intermediates are adsorbed on the PdCo surface at the fcc hollow sites with adsorption energies of -3.75 and -2.27 eV, respectively (top and side views in Figure 4e and Figure 4f). Finally, CH_4*+2H_2O* is weakly adsorbed on PdCo, as indicated by the small magnitude of its adsorption energy (-0.16 eV). Notably, in all three intermediates (CH_4*+O*+H_2O*, CH_4*+OH*+H_2O*, and CH_4*+2H_2O*), the CH_4* species preferentially adsorbs at the bridge site (Figure 4e, f, and g). We also performed van der Waals-corrected DFT calculations and updated the adsorption energy (E_{a-vdw}) in Table 2; as shown, the adsorption energies were modified by up to 0.75 eV due to the van der Waals corrections.

Furthermore, fluctuations in the zero-point energy (ZPE) of the adsorbed intermediates partially offset their adsorption stability on the PdCo surface. If the absolute magnitude of ZPE is close to or higher than that of the adsorption energy, the fluctuations will lead to mobility and desorption of the intermediates. As shown inTable 2, the adsorbed intermediates such as CH_3*+2H_2O* and CH_4*+2H_2O* are unstable and potentially mobile on the substrate surface as their ZPE values greatly exceed their adsorption energy values. In contrast, the other intermediates are broadly stable on the substrate surface.

With respect to the distances between the C and O atoms of the intermediates and the PdCo surface, the C–Pd distance of CO* is around 1.48 Å, while the average O–Pd distances of O* and OH* are around 1.40 Å and 1.8 Å, respectively (Table 2). The C–Pd of C* is 1.18 Å, and the addition of an H atom to C* to form CH* has only a small effect on the C–Pd distance. However, adding H atoms to CH* and subsequent intermediates will elongate the C–Pd distance in the following sequence: CH* (1.15 Å) < CH_2* (1.5 Å) < CH_3* (2.09 Å) < CH_4* (average ≈ 3.46 Å). This result implies a desorption tendency of these intermediates, especially CH_4*, which is consistent with the observed rather weak adsorption strength (-0.16 eV) of CH_4*+2H_2O*. Furthermore, the average bond lengths of the intermediates (i.e., C–O, C–H, and O–H) are also listed in the final column of Table 2 for reference.

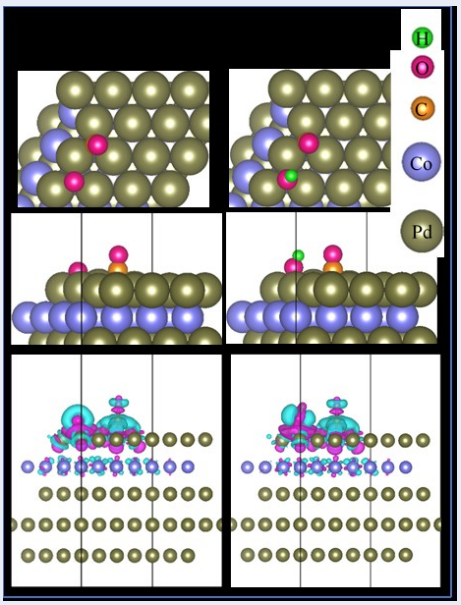

Figure 3: Schematics showing the most favorable configurations of the CO*+O* and CO*+OH* intermediates. The first, second and third rows of images present the top view, side view, and the charge density difference of each configuration, respectively. For the charge density difference plots, the isosurface value is 0.0001 $e^-/Å^{-3}$, where purple and cyan indicate electron gain and loss, respectively. The values in parentheses indicate the Bader point charge of the intermediates, where positive values signify electron accumulation.

Furthermore, based on the nudge elastic band method (Figure 5), the dissociation of CO_2* to CO*+O* and COOH* to CO*+OH* must overcome very high energy barriers due to the electronic structure contributions of 14.00 and 4.50 eV, respectively. Therefore, these dissociation processes are unfavorable. The barrier for dissociating CO_2* to CO*+O* and COOH* to CO*+OH* was calculated in three steps: (1) identification of the initial and final states (IS and FS, respectively). The initial states correspond to the most stable adsorption configurations of CO_2* and COOH* on the substrate, while the final states are CO*+O* and CO*+OH*; (2) interpolation of the transition state configuration for each dissociation pathway; and (3) application of the nudge elastic band method to optimize the previously interpolated transition state configuration. The energy barrier represents the energy difference between the transition state and the IS configurations.

We can reveal the nature of the intermediate–substrate interactions by analyzing electronic structure properties such as the Bader point charge and

Table 2: Proposed reaction intermediates with their adsorption energy without and with van der Waals corrections (E_a and E_{a-vdw}), zero-point energy (ZPE), the most stable adsorption site, the distance from the C or O atoms to the topmost Pd layer ($h_{C(O)-surf}$), and the average bond length. The information in the fourth to sixth columns was written for the main intermediates irrespective of water molecules.

Intermediate	Ea (eV)	Ea-vdw (eV)	ZPE (eV)	The adsorption site for the C or O atoms	hC(O)-surf (Å)	Average bond length (Å)
CO*+O*	-4.52	-3.77	0.25	hcp hollows	C-Pd = 1.49 O-Pd = 1.42	C-O = 1.18
CO*+OH*	-3.22	-2.57	0.49	hcp hollows	C-Pd = 1.48 O-Pd = 1.67	C-O = 1.19 O-H = 0.97
C*+2H_2O*	-4.09	-3.52	1.33	fcc hollow	C-Pd = 1.18	
CH*+2H_2O*	-4.36	-4.10	1.62	fcc hollow	C-Pd = 1.15	C-H = 1.11
CH_2*+2H_2O*	-3.10	-3.05	1.86	bridge	C-Pd = 1.50	C-H = 1.10
CH_4*+O*+H_2O*	-3.75	-3.65	1.89	bridge (hcp hollow)	C-Pd = 3.40 O-Pd = 1.39	C-H = 1.10
CH_3*+2H_2O*	-1.42	-1.46	2.15	Top	C-Pd = 2.09	C-H = 1.10
CH_4*+OH*+H_2O	-2.27	-2.40	2.17	bridge (hcp hollow)	C-Pd = 3.57 O-Pd = 1.93	C-H = 1.10 O-H = 0.97
CH_4*+2H_2O*	-0.16	-0.49	2.49	Bridge	C-Pd = 3.43	C-H = 1.10

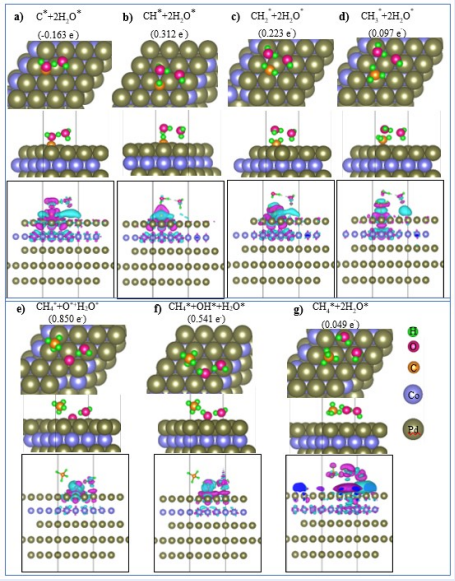

Figure 4: Atomic geometries showing the top view (first row), side view (second row), and charge density difference (third row) for CH_x* intermediates on the PdCo substrate. For the charge density difference, the isosurface value is 0.0001 $e^-/Å^{-3}$, and purple and cyan indicate electron gain and loss, respectively. The values in parentheses indicate the Bader point charge of the intermediates, where positive and negative values indicate electron accumulation and donation, respectively.

the charge density difference (Figure 3 and Figure 4). We found that all the intermediates significantly gain charge from the PdCo substrate, with the exception of C*+2H_2O*, which donates charge (0.163 e^-) to the substrate. This result implies that charge exchange dominates the interactions between the intermediates and the substrate. The charge density difference plots in Figure 3 and Figure 4 reveal that the O* and C* atoms of the intermediates are the centers of charge accumulation (purple clouds) and donation (cyan clouds), respectively.

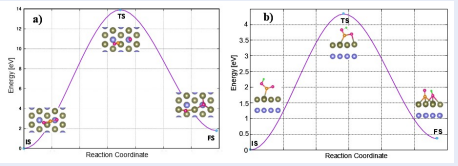

Figure 5: Minimum energy pathways for the dissociation of (a) CO_2* to CO*+ O* and (b) COOH* to CO* + OH* on the PdCo substrate. Each pathway includes the initial state (IS), transition state(TS), and final state (FS).

Thermodynamic analysis for CO_2-to-CH_4 conversion

In this section, we discuss the thermodynamics of the CM conversion process on the PdCo catalyst. The re-

action equations for all intermediates are shown in Table 1. The Gibbs free energy values for these reaction steps were calculated using formula (1), with the results listed in Table 3. For each intermediate reaction step from (R2) to (R26), the total DFT reaction energy change is calculated as the total DFT energy of the products minus that of the reactants. For example, for $CO_2^* + 4H_2 \rightarrow COOH^* + 7/2H_2$, the reaction energy change is given by $\Delta E = E[COOH/PdCo] + E[7/2H_2] - E[CO_2/PdCo] - E[4H_2]$. Here, the asterisk (*) denotes species adsorbed on the PdCo substrate. In general, the reaction energy change differs from the adsorption energy, except in cases where the products and reactants remain unchanged. For example, for $CO_2 + 4H_2 + * \rightarrow CO_2^* + 4H_2$, the reaction energy change equals the adsorption energy, i.e., $\Delta E = E[CO_2/PdCo] - E[PdCo] - E[CO_2]$, the same as equation (3). Based on the obtained Gibbs free energies, we constructed Gibbs free energy diagrams for electrode potentials of 0 and -0.549 V (Figure 6 and Figure 7, respectively). The adsorption of CO_2^* on PdCo requires a thermodynamic activation energy of 0.546 eV. The CO_2-to-CH_4 conversion process comprises two main steps, i.e., CO* formation and further hydrogenation of CO* to form the final product CH_4^*.

Figure 6 shows that CO* formation may proceed via one of three pathways: (i) the adsorption of CO_2 to form CO_2^*, (ii) the dissociation of CO_2^* to CO*+O*, or (iii) a first hydrogenation step in which CO_2^* is converted to $COOH^*$. The uphill Gibbs free energy barriers of these processes are 0.546, 1.628, and 0.549 eV, respectively. The hydrogenation of CO*+O* to form CO*+OH* proceeds spontaneously due to the downhill energy profile, whereas the dissociation of COOH* to CO*+OH* requires a small thermodynamic activation energy of 0.168 eV. However, despite the low thermodynamic barriers for dissociating CO_2^* to CO*+O* (1.628 eV) and COOH* to CO*+OH* (0.168 eV), the energy barriers are much larger due to electronic structure effects (14.0 and 4.5 eV, respectively). These large barriers indicate that these dissociation processes may be kinetically prohibited on the PdCo catalyst. The formation of CO*+H_2O* from $COOH^*$ and CO*+OH* is an exergonic process. However, to desorb CO* from CO*+H_2O*, an activation energy of 0.428 eV must be provided to reach the energy level of CO+H_2O*. The third hydrogenation of CO^* to form COH^* is more favorable than conversion to HCO*, with uphill energies of 0.492 and 0.639 eV for these processes, respectively. The conversion of COH* and HCO* to CH_2^* and CH_4^*+O* can proceed via C* and CH* formation; however, this route is considerably more expensive than the pathway via HCOH*, H_2CO^*, H_3CO^*, and CH_2OH^*. The hydrogenation steps to transform CH_2^* and CH_4^*+O* to the final product CH_4^* are exothermic and energetically favorable due to the downhill energy profile. From the above analysis, we identified the optimal paths for CM conversion, as shown by the blue arrows in Figure 6. The first path is $CO_2 \rightarrow CO_2^* \rightarrow COOH^* \rightarrow CO^* \rightarrow COH^* \rightarrow HCOH^* \rightarrow H_2COH^* \rightarrow CH_2^* \rightarrow CH_3^* \rightarrow CH_4^*$ (Path 1), with the rate-limiting step occurring at the $CO_2 \rightarrow CO_2^*$ and $CO_2^* \rightarrow COOH^*$ transformations and a maximum thermodynamic energy barrier of approximately 0.549 eV. The second favorable path passing through HCO* follows the sequence $CO_2 \rightarrow CO_2^* \rightarrow COOH^* \rightarrow CO^* \rightarrow HCO^* \rightarrow HCOH^*/H_2CO^* \rightarrow H_2COH^*/H_3CO^* \rightarrow CH_2^*/CH_4^* + O^* \rightarrow CH_3^*/CH_4^* + OH^* \rightarrow CH_4^*$ (Path 2). The rate-limiting step of Path 2 occurs at the $CO^* \rightarrow HCO^*$ conversion and the thermodynamic barrier of 0.639 eV, which is marginally higher than that of Path 1 by 0.090 eV. On the other hand, the C*-based pathway, indicated by the purple arrows in Figure 6, has a high thermodynamic barrier of 1.797 eV or 1.228 eV, with a rate-limiting step at the COH* to C* or HCOH* to CH* transformations.

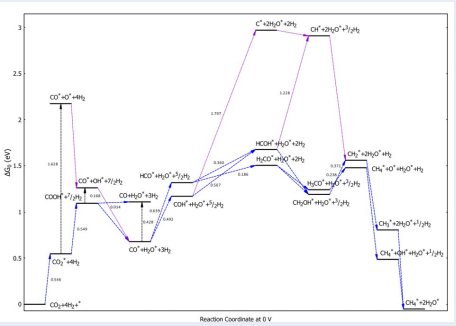

Figure 6: Free energy diagram for the CM conversion process at an electrode potential *U* of 0 V vs. RHE. The blue arrows indicate the optimal reaction pathways.

We can apply an electrode potential to reduce the thermodynamic barrier of the hydrogenation steps. Figure 7 presents the Gibbs free energy diagram for an applied potential *U* of -0.549 V vs RHE. This *U* value was identified to remove the largest thermodynamic energy barrier of the most favorable pathway (Path 1) in Figure 6. The applied potential value for the studied CM conversion process (-0.549 V vs RHE) is substan- tially lower than that required for a state-of-the-art Cu

Table 3: Gibbs free energy values for the intermediate steps listed in Table 1

No	Step	G (U=0V)	G (U=-0.549V)	No	Step	G (0 V)	G (U=-0.549V)
1	$CO_2 + 4H_2 + *$	0.000	0.000	11	$C^* + 2H_2O^* + 2H_2$	2.969	0.773
2	$CO_2^* + 4H_2$	0.546	0.546	12	$CH_2OH^* + H_2O^* + 3/2H_2$	1.191	-1.554
3	$CO^* + O^* + 4H_2$	2.174	2.174	13	$CH_3O^* + H_2O^* + 3/2H_2$	1.241	-1.504
4	$CO^* + OH^* + 7/2H_2$	1.263	0.714	14	$CH^* + 2H_2O^* + 3/2H_2$	2.907	0.162
5	$COOH^* + 7/2H_2$	1.095	0.546	15	$CH_4^* + O^* + H_2O^* + H_2$	1.479	-1.815
6	$CO^* + H_2O^* + 3H_2$	0.680	-0.418	16	$CH_2^* + 2H_2O^* + H_2$	1.561	-1.733
7	$COH^* + H_2O^* + 5/2H_2$	1.172	-0.475	17	$CH_4^* + OH^* + H_2O^* + 1/2H_2$	0.485	-3.358
8	$HCO^* + H_2O^* + 5/2H_2$	1.319	-0.328	18	$CH_3^* + 2H_2O^* + 1/2H_2$	0.803	-3.040
9	$HCOH^* + H_2O^* + 2H_2$	1.679	-0.517	19	$CH_4^* + 2H_2O^*$	-0.054	-4.446
10	$H_2CO^* + H_2O^* + 2H_2$	1.505	-0.691				

catalyst (1.04 V vs RHE), suggesting that PdCo alloy is a promising catalyst for the electrochemical reduction of CO_2 to CH_4 [3,40,41]. As shown in Figure 7, the CM conversion must overcome an uphill energy barrier of 0.546 eV, similar to the most favorable pathways (Path 1 and Path 2) in the 0 V electrode potential case. Subsequently, most of the steps proceed downhill, except for the CO^* to HCO^* step, which involves a very small energy barrier of 0.09 eV; however, this requirement is fulfilled if an activation energy of 0.546 eV is provided. Simultaneously, the applied electrode potential also reduces the thermodynamic barrier of the C*-based pathways. Note that the characteristics of the pathways remain the same in Gibbs free energy diagrams with van der Waals corrections; however, the thermodynamic energy barriers increase by 0.2 to 0.4 eV for the uphill steps compared to the case without van der Waals corrections.

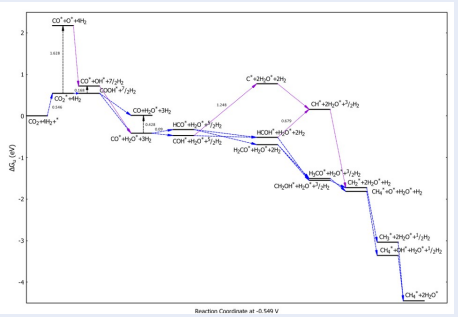

Figure 7: Free energy diagram for the CM conversion process at an electrode potential *U* of -0.549 V vs RHE. The blue arrows indicate the optimal reaction pathways.

CONCLUSIONS

In this study, the conversion of CO_2 to CH_4 on a PdCo catalyst was studied using DFT calculations coupled with a thermodynamic model. The possible intermediates and their favorable adsorption configurations were identified. Charge exchange was found to dominate the intermediate–substrate interactions. CO^* represents a key reaction intermediate, through which the most favorable transformations must pass. Two favorable CM conversion pathways were identified: (i) $CO_2 \rightarrow CO_2^* \rightarrow COOH^* \rightarrow CO^* \rightarrow COH^* \rightarrow HCOH^* \rightarrow H_2COH^* \rightarrow CH_2^* \rightarrow CH_3^* \rightarrow CH_4^*$ and (ii) $CO_2 \rightarrow CO_2^* \rightarrow COOH^* \rightarrow CO^* \rightarrow HCO^* \rightarrow HCOH^*/H_2CO^* \rightarrow H_2COH^*/H_3CO^* \rightarrow CH_2^*/CH_4^* + O^* \rightarrow CH_3^*/CH_4^* + OH^* \rightarrow CH_4^*$. These pathways can proceed with relatively low

activation energy values of 0.549 and 0.639 eV, respectively, indicating that the proposed Pd-skin/PdCo alloy is a promising catalyst for CM conversion. Regarding future work, we note that the CO_2-to-CH_4 conversion can be conducted in a gas phase or an aqueous phase. In our study, reactions (R2) to (R6) took place in the gas phase due to the absence of water molecules, whereas the other intermediate reactions occurred in an aqueous medium. Fully validating the effects of this aqueous medium is a complex and time-consuming task, which will be the focus of our next study.

COMPETING INTERESTS

The authors declare that they have no competing interests.

AUTHORS' CONTRIBUTIONS

Huynh Tat Thanh: Investigation, visualization, reviewing and editing.

Viorel Chihaia: Resources, supervision, reviewing and editing.

Do Ngoc Son: Conceptualization, formal analysis, resources, supervision, validation, writing manuscript, reviewing and editing.

ACKNOWLEDGEMENTS

This research is funded by Vietnam National University Ho Chi Minh City (VNU-HCM) under grant number VL2022-20-01.

REFERENCES

1. J A, TE M, K T, J K, R M, A S, et al. Sustainable Conversion of Carbon Dioxide: An Integrated Review of Catalysis and Life Cycle Assessment. Chemical Reviews. 2017;118:434–504. Available from: https://doi.org/10.1021/acs.chemrev.7b00435.
2. S R, J S, S M, M S, M G, J L, et al. Review on methanation – From fundamentals to current projects. Fuel. 2016 February;166:276–296. Available from: https://doi.org/10.1016/j.fuel.2015.10.111.
3. R Z, P D, P W, L Z, Q L, Y L, et al. Recent Progress in Electrocatalytic Methanation of CO2 at Ambient Conditions. Advanced Functional Materials. 2021;31. Available from: https://doi.org/10.1002/adfm.202009449.
4. L Y, L J, C Q, S Z. Electrocatalytic conversion of methane: Recent progress and future prospects. Energy Reviews. 2024;3:100065. Available from: https://doi.org/10.1016/j.enrev.2023.100065.
5. Y H, A M, K K, S S. Electrochemical reduction of carbon dioxides to carbon monoxide at a gold electrode in aqueous potassium hydrogen carbonate. Journal of the Chemical Society, Chemical Communications. 1987;728. Available from: https://doi.org/10.1039/c39870000728.
6. Y H, A M, R T. Formation of hydrocarbons in the electrochemical reduction of carbon dioxide at a copper electrode in aqueous solution. Journal of the Chemical Society, Faraday Transactions 1: Physical Chemistry in Condensed Phases. 1989;85:2309. Available from: https://doi.org/10.1039/f19898502309.
7. J C, Q Z, WY H, C C, Y L, JMP M, et al. Highly Selective Electrochemical Reduction of CO2 into Methane on Nanotwinned Cu. Journal of the American Chemical Society. 2023;145:9136–9143. Available from: https://doi.org/10.1021/jacs.3c00847.
8. Y W, C C, X Y, R W, S L, J M, et al. Enhancing CO2 electroreduction to CH4 over Cu nanoparticles supported on N-doped carbon. Chemical Science. 2022;13:8388–8394. Available from: https://doi.org/10.1039/d2sc02222b.
9. A SR, X W, J W, G L, T P, F L, et al. CO2 Electroreduction to Methane at Production Rates Exceeding 100 mA/cm2. ACS Sustainable Chemistry & Engineering. 2020;8:14668–14673. Available from: https://doi.org/10.1021/acssuschemeng.0c03453.
10. CA O, G G, J C, V G, de Arquer FP G, CT D. High-rate and selective conversion of CO2 from aqueous solutions to hydrocarbons. Nature Communications. 2023;14. Available from: https://doi.org/10.1038/s41467-023-38963-y.
11. S M, Y Y, M U. Electroreduction of CO 2 to CH 4 without overpotential using Pt-black catalysts: Enhancement of faradaic efficiency. International Journal of Energy Research. 2022;46:9919–9925. Available from: https://doi.org/10.1002/er.7836.
12. S L, HL H, F L, M G, Z Y. Electrochemical reduction of CO2 to CH4 over transition metal atom embedded antimonene: First-principles study. Journal of CO2 Utilization. 2021;51:101645.
13. and Lu R XZ, ZY L, and Tsai HJ WW, Q L, et al. Electroreduction of CO2 to methane with triazole molecular catalysts. . Nature Energy. 2024;9:1397–1406. Available from: https://doi.org/10.1038/s41560-024-01645-0.
14. N I, H S, M T, M A, N T. Methanol Synthesis from CO2Under Atmospheric Pressure over Supported Pd Catalysts. Catalysis Letters. 2004;96:75–78. Available from: https://doi.org/10.1023/b:catl.0000029533.41604.13.
15. iang H, Q G, S W, Y C, M Z. The synergistic effect of Pd NPs and UiO-66 for enhanced activity of carbon dioxide methanation. Journal of CO2 Utilization. 2019;31:167–172. Available from: https://doi.org/10.1016/j.jcou.2019.03.011.
16. L L, M W, Y C, and Wu J CZ, Y C, et al. Surface Iron Species in Palladium–Iron Intermetallic Nanocrystals that Promote and Stabilize CO2 Methanation. Angewandte Chemie. 2020;132:1454–14550. Available from: https://doi.org/10.1002/ange.201916032.
17. and Zhang L ZW, P Y, X C, H D, A L, et al. Morphological and Compositional Design of Pd–Cu Bimetallic Nanocatalysts with Controllable Product Selectivity toward CO2 Electroreduction. Small. 2017;14. Available from: https://doi.org/10.1002/smll.201703314.
18. DN S, K T. Selectivity of Palladium–Cobalt Surface Alloy toward Oxygen Reduction Reaction. . The Journal of Physical Chemistry C. 2012;116:6200–6207. Available from: https://doi.org/10.1021/jp2094615.
19. DN S, OK L, V C, K T. Effects of Co Content in Pd-Skin/PdCo Alloys for Oxygen Reduction Reaction: Density Functional Theory Predictions. . The Journal of Physical Chemistry C. 2015;119:24364–24372. Available from: https://doi.org/10.1021/acs.jpcc.5b06439.
20. Álvarez A, A B, A U, AV B, TA W, M M, et al. Challenges in the Greener Production of Formates/Formic Acid, Methanol, and DME by Heterogeneously Catalyzed CO2Hydrogenation Processes. Chemical Reviews. 2017;117:9804–9838. Available from: https://doi.org/10.1021/acs.chemrev.6b00816.
21. J Y, Cj L, D M, Q G. Methanol synthesis from CO2 hydrogenation over a Pd4/In2O3 model catalyst: A combined DFT and kinetic study. Journal of Catalysis. 2014;317:44–53. Available from: https://doi.org/10.1016/j.jcat.2014.06.002.
22. HT T, OK L, V C, DN S. Carbon dioxide conversion to methanol on a PdCo bimetallic catalyst. Physical Chemistry Chemical Physics. 2024;26:3963. Available from: https://doi.org/10.1039/d3cp05146c.
23. S C, C G, JL H, Y L, ML T, J K, et al. Free Standing Nanoporous Palladium Alloys as CO Poisoning Tolerant Electrocatalysts for the Electrochemical Reduction of CO2 to Formate. ACS Catalysis.

2019;9:5290–5301. Available from: https://doi.org/10.1021/acscatal.9b00330.
24. MT T, H P, PS L, M B, F AP. From electricity to fuels: Descriptors for C1 selectivity in electrochemical CO2 reduction. Applied Catalysis B: Environmental. 2020;279:119384. Available from: https://doi.org/10.1016/j.apcatb.2020.119384.
25. H P, MT T, X L, P SL, M B, F AP. The role of atomic carbon in directing electrochemical CO(2) reduction to multicarbon products. Energy & Environmental Science. 2021;14:473–482. Available from: https://doi.org/10.1039/d0ee02826f.
26. X L, P S, J X, Y J, L W, RB S, et al. pH effects on the electrochemical reduction of CO(2) towards C2 products on stepped copper. Nature Communications. 2019;10. Available from: https://doi.org/10.1038/s41467-018-07970-9.
27. D H, Ábel M, K B, E F, GF S, HC N, et al. CO2 Conversion on N-Doped Carbon Catalysts via Thermo- and Electrocatalysis: Role of C–NOx Moieties. ACS Catalysis. 2022;12:10127–10140. Available from: https://doi.org/10.1021/acscatal.2c01589.
28. G K, J F. Efficiency of ab-initio total energy calculations for metals and semiconductors using a plane-wave basis set. Computational Materials Science. 1996;6:15–50. Available from: https://doi.org/10.1016/0927-0256(96)00008-0.
29. G K, J H. Ab initio molecular dynamics for liquid metal. Phys Rev B. 1993;47(1):558–561. Available from: https://doi.org/10.1103/PhysRevB.47.558.
30. G K, D J. From ultrasoft pseudopotentials to the projector augmented-wave method. Phys Rev B. 1999;59(3):1758–1775. Available from: https://doi.org/10.1103/PhysRevB.59.1758.
31. JP P, K B, M E. Generalized Gradient Approximation Made Simple . Phys Rev Lett. 1996;77(18):3865–3868. Available from: https://doi.org/10.1103/PhysRevLett.77.3865.
32. M M, AT P. High-precision sampling for Brillouin-zone integration in metals. Phys Rev B. 1989;40(6):3616–3621. Available from: https://doi.org/10.1103/PhysRevB.40.3616.
33. PE B, and Andersen OK JO. Improved tetrahedron method for Brillouin-zone integrations. Phys Rev B. 1994;49(23):16223–16233. Available from: https://doi.org/10.1103/PhysRevB.49.16223.
34. HJ M, JD P. Special points for Brillouin-zone integrations. Phys Rev B. 1976;13(12):5188–5192. Available from: https://doi.org/10.1103/PhysRevB.13.5188.
35. DN S, OK L, MT H, V C. Magnetic anisotropy of ultrathin Pd 4 Co(111) film by first-principles calculations. Journal of Science: Advanced Materials and Devices. 2018;p. 243–253. Available from: https://doi.org/10.1016/j.jsamd.2018.03.004.
36. R S. Nano-catalysts for Energy Applications: CRC Press. 2021;Available from: https://doi.org/10.1201/9781003082729.
37. JK N, J R, A L, L L, JR K, T B, et al. Origin of the Overpotential for Oxygen Reduction at a Fuel-Cell Cathode. The Journal of Physical Chemistry B. 2004;17886(17892). Available from: https://doi.org/10.1021/jp047349j.
38. J H, Y Y, X L, B C, Y S, Y C, et al. Highly Selective Electroreduction of CO2 to CH4 on Cu–Pd Alloy Catalyst: the Role of Palladium-Adsorbed Hydrogen Species and Blocking Effect. Advanced Science. 2025;Available from: https://doi.org/10.1002/advs.202417247.
39. L L, T L, J X, H L, P W, D G, et al. Enhancing CO2 Electroreduction to Methane with a Cobalt Phthalocyanine and Zinc–Nitrogen–Carbon Tandem Catalyst. Angewandte Chemie International Edition. 2020;59:22408–22413. Available from: https://doi.org/10.1002/anie.202009191.
40. X N, MR E, MJ J, A A. Selectivity of CO2 Reduction on Copper Electrodes: The Role of the Kinetics of Elementary Steps. Angewandte Chemie International Edition. 2013;52:2459–2462. Available from: https://doi.org/10.1002/anie.201208320.
41. JF X, JJ C, YX H, X Z, WK W, GX H, et al. Selective electrochemical CO2 reduction on Cu-Pd heterostructure. Applied Catalysis B: Environmental. 2020;270:118864. Available from: https://doi.org/10.1016/j.apcatb.2020.118864.